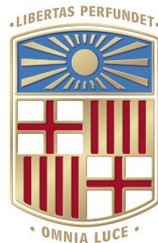

Development of a Receiver System for Passive Polarization-Encoded BB84 Protocol

Berkant Özgür Öztürk

Supervised by: Dr. José María Gómez Cama



Department of Quantum Physics and Astrophysics
University of Barcelona
Barcelona, Spain

July 6, 2025

Abstract

As the development of quantum computing threatens classical cryptographic methods, Quantum Key Distribution (QKD) provides a pathway to physically secure communication. The practical implementation of robust and efficient receiver modules, however, remains a key challenge for real world QKD systems. This thesis presents the complete design, implementation, and characterization of a high fidelity optical receiver (Bob) for the BB84 QKD protocol. The architecture is distinguished by its use of a passive random basis selection mechanism, employing a non-polarizing beam splitter to enhance system simplicity, robustness, and cost-effectiveness. Furthermore, the modular design features a fiber coupled input, ensuring flexibility for easy integration into both free-space and fiber-based quantum communication links. For polarization analysis, Wollaston prisms were selected over other alternatives due to their high extinction ratio, which is critical for minimizing measurement errors. The system was designed and optimized for an operational wavelength of 810nm for compatibility with a single photon source based on a **beta barium borate (BBO)** crystal. The receiver's performance was experimentally validated by measuring its response to a full range of input polarization states. The successful realization of this project provides a robust, flexible, and high performance receiver module suitable for deployment in further QKD experiments.

Contents

List of Figures	2
List of Tables	3
List of Abbreviations	4
1 Introduction	6
1.1 Motivation	6
1.2 Quantum Key Distribution	6
1.2.1 The No-Cloning Theorem	7
1.2.2 The BB84 Protocol	8
1.2.3 Error Correction and Privacy Amplification	10
1.3 Objectives	11
2 Theory	12
2.1 Wollaston Polarizing Prism	12
2.2 Wave Retarders	12
2.2.1 The Half-Wave Plate	13
2.2.2 The Quarter-Wave Plate	13
2.3 Optical Fibers	14
2.3.1 Multi-Mode Fiber	15
2.3.2 Single-Mode Fiber	15
2.3.3 Polarization Maintaining Fiber	15
3 Experimental Setup	16
3.1 Optical System Configuration	16
3.1.1 The Rectilinear Basis	16
3.1.2 The Diagonal Basis	17
3.2 Optical Alignment	17
3.3 Characterization of the System	18
4 Results & Discussion	19
4.1 Preliminary Characterization using a Diamond Source	19
4.2 Final Performance Validation with the BBO Source	22
5 Conclusion	24
Bibliography	25
A Light in Anisotropic Media	27
A.1 Birefringence	27
B Fiber Coupling	29

List of Figures

1	Diagram showing BB84 protocol transmission flow.	9
2	A wollaston polarizing prism spatially separates an input beam into two orthogonally polarized components, the ordinary and extraordinary ray, using two birefringent wedges with perpendicular optic axes. Adapted from [15].	12
3	Rotation of linearly polarized light using a half-wave plate (HWP). An input polarization oriented at an angle θ to the fast axis is rotated by an angle of 2θ after passing through the plate. Adapted from [11].	13
4	Schematic showing the conversion of linear to circular polarization. When linearly polarized light is incident on a quarter-wave plate (QWP) at an angle of 45° to its fast axis, the exiting beam becomes circularly polarized. Adapted from [11].	14
5	Comparison of multi-mode fiber (MMF) and single-mode fiber (SMF). Adapted from [16].	14
6	PANDA type polarization maintaining fiber (PMF). (a) The fiber's cross section, illustrating the two stress rods placed alongside the core. (b) A depiction of the resulting phase retardation between orthogonal field components caused by the stress induced birefringence. Adapted from [16].	15
7	Initial design schematic of the receiver optical system.	16
8	The final experimental receiver shown in its testing configuration. This photograph shows the completed optical setup with additional components, such as the input linear polarizer used to simulate signals from Alice, installed for system characterization.	18
9	The graph shows the experimentally measured second-order autocorrelation function, $g^{(2)}(\tau)$, as a function of the time delay, τ	20
10	The plot shows the normalized count rates for the four detection ports as the input linear polarization is rotated through 360° . The data shown was obtained using the photon source based on nitrogen-vacancy (NV) centers.	21
11	The graph compares the measured signal photon counts (with the BBO source active) to the intrinsic dark counts (with the source blocked) for each of the four output detection channels.	22
12	The plot shows the normalized count rates for the four detection ports as the input linear polarization is rotated through 360° . The data shown was obtained using the single photon source based on BBO crystal.	23
13	Index ellipsoid. Adapted from [15].	29
14	Focusing a Gaussian beam into a single mode fiber using a lens of focal length f	30
15	The acceptance angle and general structure of an optical fiber. The diagram shows the fiber's core and cladding, and illustrates the maximum acceptance angle, θ_{max} . Adapted from [11].	31

List of Tables

1	Encoding scheme of classical bits on polarization states in two different orthogonal bases.	8
2	The BB84 key distribution protocol.	10
3	Calculated coupling efficiencies of the system's ports for both cases, when a MMF and a PMF were used at the input.	19

List of Abbreviations

- APD** avalanche photodiode. 18, 22
- BBO** beta barium borate. 1, 2, 11, 16, 18, 22–24
- BPF** bandpass filter. 17
- BS** beam splitter. 11, 16, 18, 20, 24
- HBT** Hanbury Brown and Twiss. 20
- HWP** half-wave plate. 2, 13, 16, 17
- MFD** mode field diameter. 30, 31
- MMF** multi-mode fiber. 2, 3, 14, 15, 17–19, 22, 29
- NA** numerical aperture. 15, 30
- NV** nitrogen-vacancy. 2, 19–21
- PBS** polarizing beam splitter. 17, 24
- PMF** polarization maintaining fiber. 2, 3, 14–17, 19
- QBER** quantum bit error rate. 6, 9, 11, 17
- QKD** quantum key distribution. 6, 7, 11, 16, 17, 20, 23, 24
- QWP** quarter-wave plate. 2, 13, 14, 16
- SMF** single-mode fiber. 2, 14, 15, 19, 29, 31
- SPDC** spontaneous parametric down conversion. 16, 18
- TIR** total internal reflection. 14, 30

WPP wollaston polarizing prism. [2](#), [12](#), [16](#), [17](#), [22](#), [24](#)

1 Introduction

The increasing reliance on digital communication has made information security a paramount concern. For decades, the security of sensitive data has been guaranteed by classical cryptographic protocols, such as RSA, which rely on the computational difficulty of mathematical problems like integer factorization. However, the prospective development of large scale quantum computers, powered by algorithms such as Shor's, threatens to render these conventional cryptographic systems obsolete, creating an urgent need for a new generation of secure communication technologies. In response to this threat, **quantum key distribution (QKD)** has emerged as a revolutionary paradigm, offering security based not on computational assumptions, but on the fundamental and immutable laws of quantum mechanics.

Among the various **QKD** protocols, the one proposed by Charles Bennett and Gilles Brassard in 1984 [3], famously known as BB84, remains the most foundational and widely studied in the field. The BB84 protocol's security relies on encoding information onto the quantum state of single photons. Specifically, classical bits are encoded using four distinct polarization states, which are grouped into two mutually unbiased bases. The security of the distributed key is guaranteed by the quantum mechanical principle that a measurement on a state from one basis will irreversibly disturb it if the incorrect basis is chosen, an effect that would reveal the presence of an eavesdropper. The protocol therefore requires that the receiver (Bob) independently and randomly select one of the two bases for measuring each incoming photon sent by the transmitter (Alice).

1.1 Motivation

The successful implementation of a BB84 **QKD** protocol hinges on the performance of its receiver module. This component must provide a precise and reliable mechanism for choosing a measurement basis at random and for accurately analyzing the four possible incoming polarization states. Every architectural decision, from the basis selection strategy to the choice of polarization optics, has a direct bearing on essential system metrics like the secure key rate and the **quantum bit error rate (QBER)**. The research in this thesis was therefore guided by the goal of creating a receiver design that effectively meets these implementation challenges.

1.2 Quantum Key Distribution

In secure communication, two entities aim to safeguard their exchanges from third-party interference. This encompasses confidentiality, ensuring that unauthorized entities cannot acquire information from transmitted messages, and authentication, which enables a recipient to verify the integrity and origin of a message. Traditionally, these objectives require the prior agreement of a secret key. However, achieving secure key distribution through purely classical communication channels is unfeasible without additional underlying assumptions. In contrast, the **QKD** leverages the principles of quantum mechanics to establish a secure and continuous generation of secret keys, thereby enabling robust secure communication.

After the hurdle of secure key distribution is overcome, the message can be encrypted using a classical cryptographic protocol, such as the one-time pad, which is provably secure. For messages $m \in M$ of bit length n that Alice wishes to send to Bob, a random private

key, with the same length as the message and shared beforehand between the two parties using QKD, will be used to initiate the encryption process [6]. The procedure is as follows:

1. Firstly, the ciphertext c is computed by applying a bitwise exclusive OR operation (XOR) between the message m and the private key k , such that $m \oplus k = c$.
2. Then, the ciphertext c is sent through the public channel to Bob.
3. Finally, the message m is recovered by applying the bitwise XOR operation between the ciphertext c and the private key k , such that $c \oplus k = (m \oplus k) \oplus k = m$.

It is crucial to note that employing the same private key for encrypting distinct messages leads to a significant cryptographic weakness, potentially enabling the decryption of those messages [6].

There are two main schemes to implement quantum key distribution: the "prepare-and-measure" and the "entanglement-based" schemes. This work will focus only on the "prepare-and-measure" scheme, as our research is based on it. In this scheme, classical bits are encoded onto a set of non-orthogonal quantum states. This non-orthogonality ensures that if an eavesdropper intercepts the channel, the quantum states cannot be perfectly distinguished [2]. Furthermore, the security of the key distribution is reinforced by the no-cloning theorem, which ensures that an adversary cannot copy the quantum state to gain complete information about the quantum state.

1.2.1 The No-Cloning Theorem

The security of quantum key distribution is fundamentally guaranteed by the No-Cloning theorem, which was introduced by Wootters and Zurek [17]. The theorem's foundation lies in two core principles of quantum mechanics: that the evolution of a closed system is a unitary transformation, and that this transformation is linear [2]. Consequently, the No-Cloning theorem asserts the impossibility of creating an identical copy of an arbitrary, unknown quantum state.

Let U be an unitary transformation that copies the basis state $|0\rangle$ and $|1\rangle$ of a two-level system perfectly to an arbitrary initial state $|i\rangle$ such that,

$$U |0\rangle |i\rangle = |0\rangle |0\rangle \tag{1}$$

$$U |1\rangle |i\rangle = |1\rangle |1\rangle \tag{2}$$

If we apply U to an unknown state $|\psi\rangle = \alpha |0\rangle + \beta |1\rangle$, where $|\alpha|^2 + |\beta|^2 = 1$, we obtain the following relation,

$$U |\psi\rangle |i\rangle = U(\alpha |0\rangle + \beta |1\rangle) |i\rangle \quad (3)$$

$$= \alpha |0\rangle |0\rangle + \beta |1\rangle |1\rangle \quad (4)$$

$$\neq |\psi\rangle |\psi\rangle \quad (5)$$

Therefore, an unknown quantum state $|\psi\rangle$ cannot be copied perfectly. The No-Cloning theorem is one of the most significant properties that quantum mechanics provides for secure communication. An adversary cannot exploit the quantum system to copy the transmitted information, in contrast, this is trivial to achieve in classical communication.

1.2.2 The BB84 Protocol

The BB84 protocol, developed by Bennett and Brassard in 1984 [3], represents the foundational method for quantum key distribution. The protocol is based on a prepare-and-measure scheme where classical bits are encoded onto a two-level quantum system. This system is physically realized using the polarization states of single photons. For the encoding, two mutually unbiased bases are employed: the rectilinear (\oplus) and the diagonal (\otimes). The fundamental property of these mutually unbiased bases is that the overlap probability of any state from one basis with any state from the other is $1/2$, e.g. $|\langle V|D\rangle|^2 = \frac{1}{2}$. This orthogonality condition ensures that if a measurement is performed in the incorrect basis, the outcome is completely random, yielding no information about the originally encoded bit [12].

The specific encoding is as follows:

- In the rectilinear basis (\oplus), the classical bits '0' and '1' are encoded as the horizontal ($|H\rangle$, 0°) and vertical ($|V\rangle$, 90°) polarization states, respectively.
- In the diagonal basis (\otimes), '0' and '1' are encoded as the diagonal ($|D\rangle$, 45°) and anti-diagonal ($|A\rangle$, 135°) states, respectively.

This encoding scheme is summarized in Table 1.

	0	1
\oplus	$ H\rangle$	$ V\rangle$
\otimes	$ D\rangle$	$ A\rangle$

Table 1: Encoding scheme of classical bits on polarization states in two different orthogonal bases.

In order to establish the protocol, the following steps are followed:

1. **State Preparation and Transmission:** For each bit of a secret key Alice wishes to send, she generates two random bits: one representing the key bit itself and the other determining the transmission basis. She then encodes each key bit onto a single photon using the polarization state dictated by her basis choice. This process

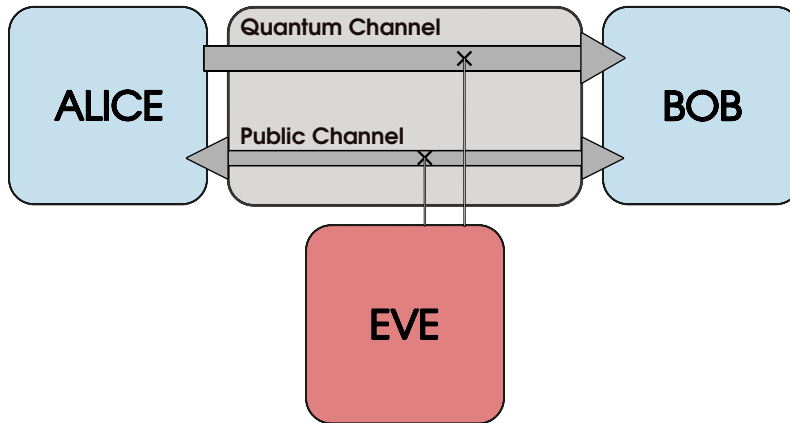


Figure 1: Diagram showing BB84 protocol transmission flow.

is repeated to create a sequence of polarized photons, which are then transmitted to Bob over a quantum channel.

2. **Measurement:** For each photon he receives, Bob independently and randomly selects a measurement basis and records the resulting bit value. Due to the random and independent choices, Bob's measurement basis will match Alice's preparation basis for any given photon with a probability of 50%. In cases of a basis mismatch, Bob's measurement outcome will be completely uncorrelated with Alice's original key bit, as detailed in Table 2.
3. **Basis Reconciliation:** Following the quantum transmission, Alice and Bob communicate over an authenticated public classical channel. They publicly announce the sequence of bases they each used for every photon. It is critical that they do not reveal the actual bit values during this step.
4. **Key Sifting:** Alice and Bob compare their basis sequences and discard all bits for which their bases did not match. The remaining subset of bits, where they used the same basis, is known as the **sifted key**. At this stage, in an ideal scenario, their sifted keys are identical. This process is illustrated in Table 2.
5. **Error Rate Estimation:** To verify the security of the channel, Alice and Bob publicly compare a randomly selected subset of their sifted key bits. By calculating the discrepancy rate, known as the **QBER**, they can estimate the amount of information potentially intercepted by an eavesdropper. These publicly revealed bits are then discarded from the key.
6. **Security Check:** If the measured **QBER** is below a predetermined security threshold, they conclude that the key is secure enough to proceed. If the error rate is too high, they abort the protocol and attempt a new transmission.
7. **Error Correction and Privacy Amplification:** Two final procedures are performed on the remaining sifted key bits:

- **Error Correction:** A classical error correction protocol is run to identify and remove any discrepancies in Alice’s and Bob’s keys, ensuring they possess identical bit strings.
- **Privacy Amplification:** This process distills a shorter, but cryptographically secure, final key from their corrected key. It reduces any partial information that Eve might have gained about the key to a negligible amount [2].

Alice’s string	1	1	0	1	0	0	1	0	1	1	1	1	0	0
Alice’s basis	\oplus	\oplus	\oplus	\otimes	\otimes	\oplus	\otimes	\otimes	\otimes	\otimes	\oplus	\oplus	\oplus	\oplus
Bob’s basis	\oplus	\otimes	\oplus	\oplus	\otimes	\oplus	\otimes	\oplus	\otimes	\otimes	\oplus	\oplus	\oplus	\oplus
Bob’s string	1	R	0	R	0	0	1	R	1	1	1	1	0	0
Same basis?	Y	N	Y	N	Y	Y	Y	N	Y	Y	Y	Y	Y	Y
Sifted bits	1		0		0	0	1		1	1	1	1	0	0
Test	Y		N		N	Y	N		N	N	N	Y	Y	N
Private key			0		0		1		1	1	1			0

Table 2: The BB84 key distribution protocol.

The entire process is conceptually illustrated by the diagram in Fig. 1.

A critical requirement for the BB84 protocol is that the public channel connecting Alice and Bob must be authenticated, although it does not need to be confidential [10]. Authentication is essential to guarantee that Alice and Bob are communicating with each other and not an adversary. This process of authentication presupposes the existence of a secret key shared between the parties before the protocol begins. This initial key may be established through any secure method, such as physical exchange. Therefore, the BB84 protocol assumes the prior establishment of an authenticated public channel.

1.2.3 Error Correction and Privacy Amplification

Following the initial key sifting process, Alice and Bob must ensure their key strings are perfectly identical. This is achieved through a classic post-processing step known as error correction. The primary objective of this phase is to identify and eliminate any discrepancies between their respective keys that may have been introduced by channel noise or the presence of an eavesdropper [2]. To accomplish this, Alice and Bob engage in a public discussion about certain properties of their key bits without revealing the entire key itself. For instance, they might compare the parity (XOR value) of randomly chosen subsets of their bits [10]. Based on this public exchange, they can locate and discard the erroneous bits from their sequences. This process inherently shortens the key but results in two identical copies shared between the legitimate parties [10]. However, even after this correction, it is assumed that an eavesdropper may still possess partial information about this newly reconciled key.

After establishing an identical key through error correction, Alice and Bob must address the residual information that an eavesdropper may have acquired. This is the purpose of privacy amplification, a procedure designed to reduce Eve’s knowledge to a negligible level. Unlike error correction, this process is performed locally. Alice and Bob agree publicly on a set of operations, for instance, which pairs of bits to combine using an XOR

function, but they do not announce the results [10]. They each independently apply these operations to their identical keys to produce a new, shorter one. The security of this method lies on a fundamental principle: partial information on a set of bits translates to even less information about their combined result. For example, if Eve knows the value of two separate bits with only a certain probability, her probability of correctly guessing their XOR value is significantly lower [10]. By repeating this process or using more advanced algorithms on larger blocks of data, Alice and Bob can distill a final, shorter key about which Eve has virtually no information, thus ensuring its cryptographic security.

1.3 Objectives

To address the practical challenges in the implementation of the optical receiver (Bob), the research presented in this thesis was guided by the following key objectives:

- To design and implement a passive receiver architecture where the random basis selection for the BB84 protocol is achieved using a non-polarizing **beam splitter (BS)**. The goal is to create a system that is inherently robust, cost-effective, and does not require active modulation or external random number generators.
- To investigate and select high performance polarization splitting optics to ensure high fidelity measurements. This involved a deliberate design choice to employ Wollaston prisms, justified by their superior extinction ratio and ability to provide high purity separation of polarization states, which is critical for minimizing the **QBER**.
- To perform the final system characterization using single photons generated from a **BBO** crystal. This validation involved experimentally measuring the dependence of the output port count rates on the input polarization state to confirm the receiver's adherence to theoretical predictions.
- To build the receiver with a modular and flexible design that ensures its future applicability. The architecture was intentionally designed to be adaptable for use in various experimental contexts, including both free-space and fiber-based **QKD** systems, and to be compatible with different single photon sources.

The successful fulfillment of these objectives is detailed in the subsequent chapters of this thesis.

2 Theory

2.1 Wollaston Polarizing Prism

The **wollaston polarizing prism (WPP)** is a polarizing beam splitter designed to separate an incident, unpolarized beam of light into two orthogonally polarized beams [1]. While these prisms are typically fabricated from either quartz or calcite crystals [11], the one utilized in this work is made of calcite. It is constructed by cementing together two triangular calcite prisms such that their respective optic axes are oriented perpendicularly to one another.

When a light beam enters the prism at normal incidence, it initially travels undeviated. Within the first section of the prism, the beam splits into two components due to birefringence (see Appendix A.1): the ordinary ray, which is polarized perpendicular to the optic axis and experiences a refractive index of n_o , and the extraordinary ray, polarized parallel to the optic axis and subject to the principal index n_e , as shown in Fig. 2. Consequently, upon reaching the internal interface, the identities of the rays are inverted. The original ordinary ray now propagates as an extraordinary ray in a medium of lower refractive index (n_e) and is refracted away from the normal. Conversely, the original extraordinary ray becomes an ordinary ray, enters a medium of higher refractive index (n_o), and bends toward the normal. As both rays finally exit the prism, they are refracted away from the normal again, which further increases their angular divergence [1].

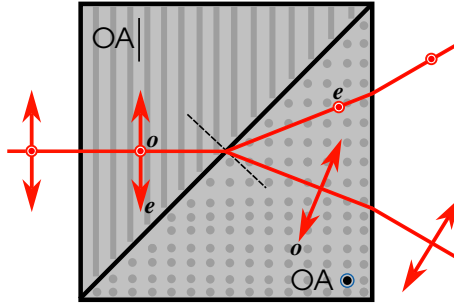


Figure 2: A **wollaston polarizing prism** spatially separates an input beam into two orthogonally polarized components, the ordinary and extraordinary ray, using two birefringent wedges with perpendicular optic axes. Adapted from [15].

Wollaston prisms are characterized by a high extinction ratio. This property allows them to separate an incident beam into two components that exhibit both high polarization purity and high transmittance. Consequently, these prisms are highly suitable for polarization sensitive applications, where precise control over the polarization state is essential [8].

2.2 Wave Retarders

An optical retarder is a component designed to modify the polarization state of light by introducing a controlled phase difference between its orthogonal electric field components. This effect is typically achieved using an anisotropic crystal, which possesses a structurally dependent refractive index. Due to this anisotropy, the crystal exhibits two principal axes: a fast axis with a lower refractive index (n_f) and a slow axis with a higher refractive index (n_s) [11].

When polarized light passes through such a material, its electric field components aligned with these axes propagate at different velocities. This difference in speed results in an accumulation of a relative phase shift between the two components as they traverse the crystal. The magnitude of this phase shift, known as the retardation (Γ), determines the final polarization form of the exiting beam [15]. The retardation is directly proportional to the relative optical path length difference between the two components and is the key parameter describing the component's effect on polarization,

$$\Lambda = d(|n_s - n_f|) \quad (6)$$

where d is the thickness of the material [11]. The retardance, Γ , is therefore given by the expression:

$$\Gamma = \frac{2\pi}{\lambda_0} d(|n_s - n_f|) \quad (7)$$

Although a wave retarder can in principle be designed to produce any arbitrary phase shift, two specific retarders find the broadest application, the **half-wave plate** and the **quarter-wave plate**.

2.2.1 The Half-Wave Plate

A **half-wave plate** functions by introducing a relative phase difference of π radians between two orthogonal electric field components. The primary effect of this phase shift is a rotation of the light's polarization state. For instance, if linearly polarized light is incident on a **HWP** at an angle θ relative to the fast axis, its plane of polarization will be rotated by an angle of 2θ upon exiting the plate [11]. This transformation is illustrated in Fig. 3. Furthermore, a **HWP** acts as a polarization rotator for any incident polarization state. For

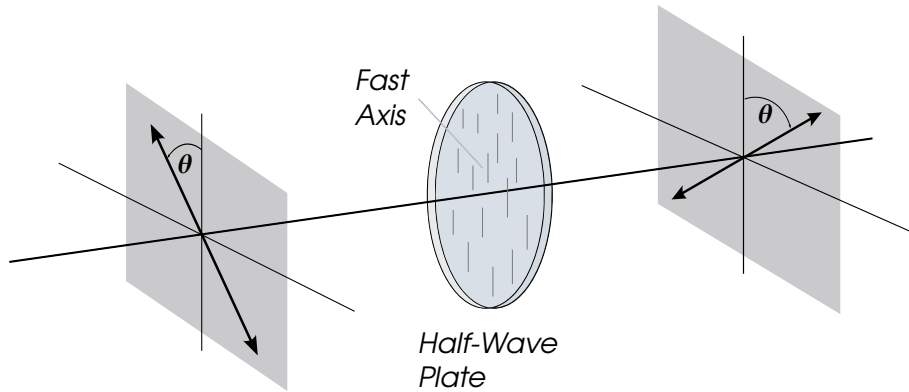


Figure 3: Rotation of linearly polarized light using a **HWP**. An input polarization oriented at an angle θ to the fast axis is rotated by an angle of 2θ after passing through the plate. Adapted from [11].

instance, in the case of circularly or elliptically polarized light, it reverses the polarization's handedness, converting a right-handed state to left-handed and vice versa [11].

2.2.2 The Quarter-Wave Plate

A **quarter-wave plate** introduces a relative phase difference of $\pi/2$ radians between orthogonal electric field components. Its primary function is to convert linearly polarized light into elliptically polarized light, and conversely, elliptical into linear. A notable special case

occurs when the incident linear polarization is oriented at an angle of 45° to the fast axis; in this specific configuration, the output beam becomes circularly polarized, as depicted in Fig. 4. However, if the incident light's polarization is perfectly aligned with either the fast or slow axis, it passes through the QWP without any change to its polarization state.

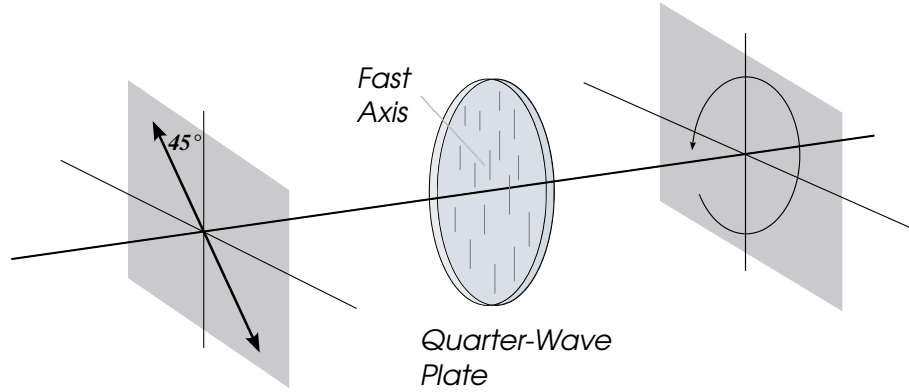
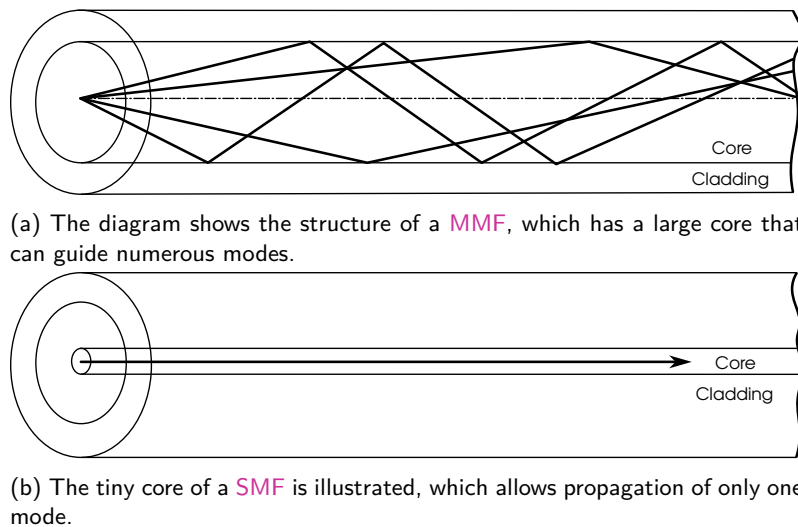


Figure 4: Schematic showing the conversion of linear to circular polarization. When linearly polarized light is incident on a QWP at an angle of 45° to its fast axis, the exiting beam becomes circularly polarized. Adapted from [11].



(a) The diagram shows the structure of a MMF, which has a large core that can guide numerous modes.

(b) The tiny core of a SMF is illustrated, which allows propagation of only one mode.

Figure 5: Comparison of MMF and SMF. Adapted from [16].

2.3 Optical Fibers

Optical glass fibers are fundamental components in modern optics that serve as waveguides to confine and transmit light, particularly in applications such as optical communications. The guiding mechanism is based on the phenomenon of total internal reflection (TIR). This is achieved through a structure comprising a central core with a refractive index (n_f) surrounded by a cladding material with a slightly lower refractive index (n_c) [15]. When light propagating within the core strikes the core cladding interface at an angle of incidence greater than the critical angle (θ_c), it undergoes TIR. This process of repeated reflection confines the light to the core, allowing it to be guided along the length of the fiber with minimal loss. Different applications necessitate the use of various types of fibers, including MMFs, SMFs, and PMFs, the properties of which will be discussed in the subsequent sections.

2.3.1 Multi-Mode Fiber

A **multi-mode fiber** is a type of optical waveguide designed to support the simultaneous propagation of many different light paths, or modes. This capability is a direct result of its large core diameter (see Fig. 5a). A significant consequence of this multi modal propagation is that each mode traverses a unique path length, resulting in variations in their propagation times along the fiber. This phenomenon, known as modal dispersion, becomes more pronounced as the core diameter increases, since a larger core can accommodate a greater number of modes [11].

2.3.2 Single-Mode Fiber

A **single-mode fiber**, depicted in Fig. 5b, utilizes an extremely narrow core, less than $10\mu\text{m}$, to restrict light propagation to a single fundamental mode, thereby eliminating modal dispersion [11]. While this property is highly desirable for many applications, it comes at the cost of increased coupling difficulty, a complication that is further magnified by the lower **numerical aperture (NA)** typical of such fibers.

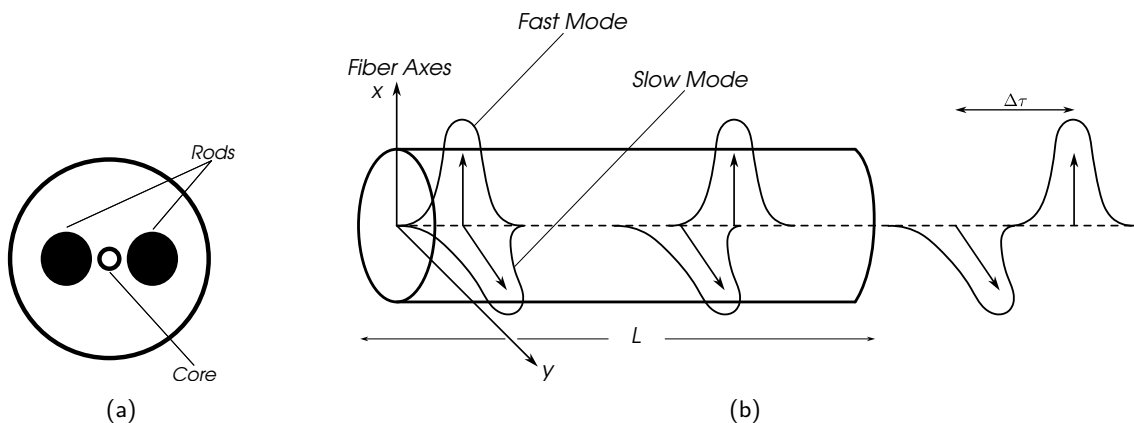


Figure 6: PANDA type **PMF**. (a) The fiber's cross section, illustrating the two stress rods placed alongside the core. (b) A depiction of the resulting phase retardation between orthogonal field components caused by the stress induced birefringence. Adapted from [16].

2.3.3 Polarization Maintaining Fiber

Unlike standard optical fibers that are susceptible to polarization scrambling from environmental stress, **PMFs** are designed to preserve the polarization of transmitted light. This is accomplished by inducing a strong internal birefringence, as seen in the PANDA type fibers used in this work, which feature two stress applying rods alongside the core (see Fig. 6a) [16]. This structure establishes two principal axes (fast and slow), and light polarized along either axis will maintain its state during propagation. However, the polarization maintaining property of the fiber is effective only when the input light is precisely aligned with one of its principal axes. If the input polarization is misaligned, it will be resolved into components along both the fast and slow axes. Due to the fiber's birefringence, these two components propagate at different phase velocities, resulting in an accumulated relative phase difference along the fiber's length, a process illustrated in Fig. 6b. This induced phase shift alters the light's overall state of polarization, for instance, converting an initial linear state into an elliptical one. Consequently, an external polarization control system is required to compensate for the effects of any imperfect input alignment.

3 Experimental Setup

The optical configuration of the receiver system is depicted in Fig. 7. The system is designed to be part of free-space BB84 QKD system, which the information is passively encoded onto photons generated from the BBO crystal by the process of spontaneous parametric down conversion (SPDC). The wavelength of the emitted photons is 810nm. The photons are sent from the transmitter (Alice) through a telescope, traverse a free-space link, and are collected by a second telescope at the receiver (Bob). The collected optical signal is then coupled into a PMF cable and directed to the detection module for analysis.

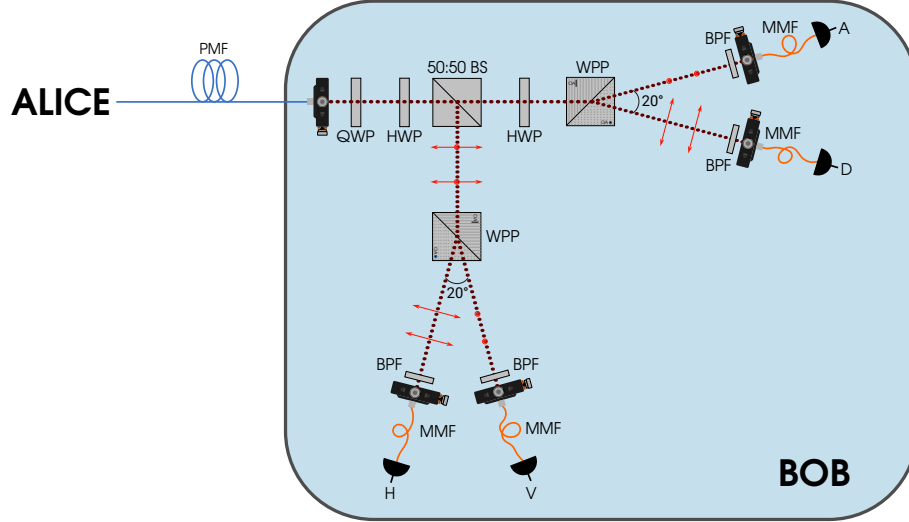


Figure 7: Initial design schematic of the receiver optical system.

3.1 Optical System Configuration

As depicted in Fig. 7, the receiver's optical path begins with the input signal arriving via a PMF. The light is first collimated into a free-space beam by a fiber coupler, which is mounted on a XY translation stage for precise alignment. Following collimation, the beam passes through a polarization correction stage consisting of a QWP and a HWP. This stage is necessary because a PMF is a birefringent medium, and any misalignment between the input light and the fiber's axes can induce a phase shift, altering the signal's polarization state, for instance, making it elliptical. The QWP is used to compensate for this ellipticity, restoring a linear polarization state. Subsequently, the HWP rotates this corrected linear polarization to match the orientation that was originally encoded at Alice's side.

A non-polarizing BS then randomly directs each photon to one of two measurement paths, reflecting approximately 50% and transmitting the rest. This probabilistic action serves as the random basis selection mechanism for the BB84 protocol, routing photons to be measured in either the rectilinear (\oplus) basis via the reflection path or the diagonal (\otimes) basis via the transmission path.

3.1.1 The Rectilinear Basis

In the reflected branch of the setup, as illustrated in Fig. 7, photons first encounter a WPP. This component separates the beam according to its polarization, causing the horizontally

and vertically polarized photons to propagate at a 20° angle relative to each other. A critical design decision was the choice of component for splitting the beam based on its polarization. For this task, a **WPP** was selected over a **polarizing beam splitter (PBS)**. This choice was motivated by the significantly higher extinction ratio offered by the **WPP**. A higher extinction ratio ensures greater polarization purity in the separated beams, which is essential for minimizing the **QBER** in the **QKD** system. Following the prism, two mirrors direct each of these polarized beams into one of two separate collection ports (see Fig. 8). Each port is equipped with a **bandpass filter (BPF)** that allows only photons within a 40nm bandwidth centered at 800nm to pass, a range suitable for the 810nm signal photons. Finally, the filtered light is launched via a fiber coupler into a **MMF**, which guides the photons to the single photon detector.

3.1.2 The Diagonal Basis

The transmitted branch of the setup is designed to perform measurements in the diagonal basis. However, the **WPP** used for polarization analysis can only separate horizontal and vertical components. Therefore, to enable measurement of the diagonal basis, a **HWP** is placed in the beam path after the main beam splitter. The function of this **HWP** is to rotate the diagonal basis states into the rectilinear basis, converting diagonally and anti-diagonally polarized photons into horizontally and vertically polarized photons, respectively. This is achieved by setting the fast axis of the **HWP** at an angle of 22.5° relative to the incident diagonal polarization, which induces the required 45° rotation, as illustrated in Fig. 3. Without this rotation, diagonally and anti-diagonally polarized photons would be indistinguishable, as they would be split with equal probability by the **WPP**. Following this component, the rest of the setup is identical to the reflected branch.

3.2 Optical Alignment

Aligning the optical system presented a practical challenge, as the single photon source used for the experiments is not visible, rendering initial, coarse alignment of the beam path infeasible. As is common practice for such systems, a visible source was required as stated in Benton [4]. For this purpose, a red alignment laser operating at the wavelength of 635nm was used to establish and optimize the optical path before introducing the single photon source.

To couple the alignment laser into the system’s input **PMF**, a two step procedure was employed to simplify the otherwise difficult alignment. First, the laser was coupled into a **MMF**, which has a larger core diameter and is easier to work with. Once this initial coupling was maximized, the **MMF** was replaced with the final **PMF**, and the alignment was fine tuned.

With the visible beam propagating through the system, the free-space optical components were then aligned. This process was particularly focused on the most critical part of the alignment, efficiently coupling the light into the fibers at each of the four output ports. A notable complication during this procedure was the significant optical loss observed, which occurred because the anti-reflection coatings on the optical elements were optimized for the 810nm experimental wavelength, not the wavelength of the red alignment laser. To correct for any residual misalignment caused by this discrepancy, the output fiber couplings were carefully optimized again using the actual single photon source immediately before

each characterization measurement was performed.

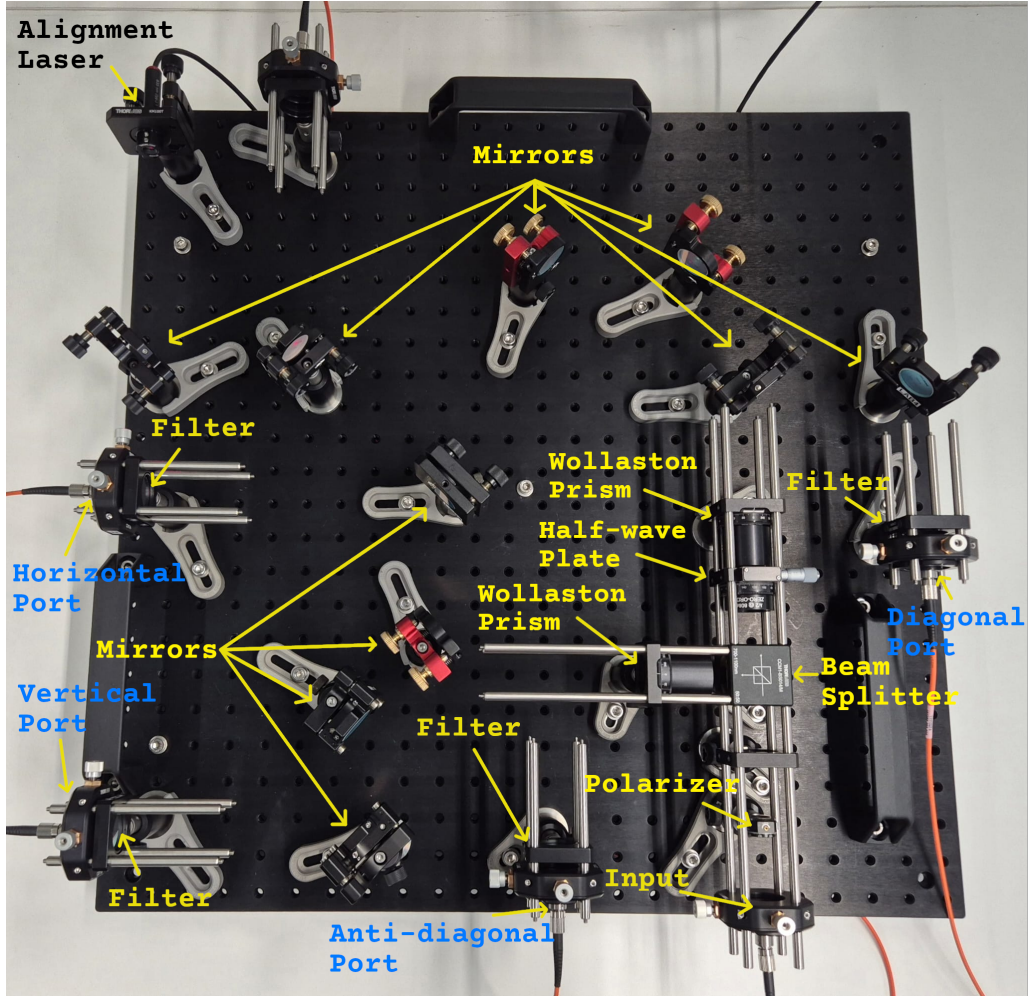


Figure 8: The final experimental receiver shown in its testing configuration. This photograph shows the completed optical setup with additional components, such as the input linear polarizer used to simulate signals from Alice, installed for system characterization.

3.3 Characterization of the System

The performance of the fully assembled receiver, shown in the photograph in Fig. 8, was experimentally characterized. To achieve this, the polarization encoding performed by Alice was simulated by placing a linear polarizer in the input beam path, just before the BS. The core of the characterization involved measuring the photon count rates at each of the four output ports as a function of the input polarizer’s orientation, which was rotated systematically in 10° increments. This measurement procedure was conducted using two different single photon sources. The system was first tested using photons generated by optical centers in diamond, which were delivered to the receiver’s input via a MMF. Following this, a final validation was performed by repeating the characterization with the single photon source for which the receiver was specifically designed, 810 nm photons generated from a BBO crystal via the SPDC process. This second series of measurements confirmed the receiver’s performance under its intended operational conditions. Photon detection for the four output ports is performed using a 4-channel silicon avalanche photodiode (APD) module from Excelitas (SPCM-AQ4C). The electronic signals from the APD are then processed by a time tagger from Swabian Instruments (Time Tagger Ultra).

4 Results & Discussion

Achieving high fiber coupling efficiency was one of the most critical factors affecting the overall performance of the system. As noted in Section 3.2, we used **MMFs** for the initial system alignment. We chose **MMFs** for the input port because it's significantly easier to couple light into their larger cores compared to **SMFs**. This approach ensured we had sufficient optical power throughout the entire system, which made the alignment process much more manageable. Afterwards, we performed the fiber coupling at each of the four output ports. Throughout all stages of testing, the quality of the coupling at each port was quantified by its efficiency, which was calculated using the following simple relation,

$$efficiency = \frac{P_{out}}{P_{in}} \times 100 \quad (8)$$

In the Eq. (8), P_{in} is the optical power measured at the input of the fiber before the coupling, and P_{out} is the power measured at the output of the fiber after light propagates through it. Furthermore, the fiber coupling efficiency of the red alignment laser to the **MMF** was **56 %**. Following that, coupling of the laser beam to each of the four ports were established. In this process, for the precise control of the system behavior and to estimate the losses in every step, optical power was measured after every element along the path of the beam. The exact same procedure was also performed with coupling the alignment laser to the **PMF**. In the case of **PMF**, the coupling process was very tedious since there is a single core in it which is significantly narrower than the **MMF**. Also, specifically in **PMFs** there are two rods that sandwich the core to induce stress along one axis of the core to be able to maintain the input polarization of light when it is aligned properly with its axis. While coupling to the **PMF** the process was very sensitive to any type of disturbance, for instance, even a slight touch to the mirror knobs was effecting the power readings in the power meter dramatically. After all, the coupling efficiency that is achieved with the **PMF** was **13.8 %**. The calculated fiber coupling efficiencies for each of the four output ports are presented in Table 3.

	MMF	PMF
Vertical Port	97.3 %	85.2 %
Horizontal Port	90.5 %	88 %
Diagonal Port	88.5 %	91.3 %
Anti-diagonal Port	92.2 %	95.4 %

Table 3: Calculated coupling efficiencies of the system's ports for both cases, when a **MMF** and a **PMF** were used at the input.

4.1 Preliminary Characterization using a Diamond Source

Due to initial practical limitations, the system's characterization was first performed using single photons generated by exciting **NV** centers in nanodiamonds, as this experimental setup was readily available at the time. The **nitrogen-vacancy** center is a prominent emitter in diamond, characterized by its high quantum efficiency at room temperature and its excellent optical stability. Despite its advantages, the **NV** center has a significant limitation arising from its strong electron-phonon coupling. This interaction results in a spectrally broad emission, spanning a wavelength range from 600 to 850nm [14]. Furthermore, the

intrinsically long excited state lifetime of the NV center prevents the emission of single photons at high repetition rates. This limitation, combined with the spectral broadening mentioned previously, may therefore prevent the NV center from being a viable source for practical quantum communication systems [14]. However, for our purposes, the broad emission spectrum of the NV centers proved to be advantageous. Its wide spectral range conveniently overlapped with the receiver’s designed operational wavelength of 810nm. Although this source was not ideal for a complete characterization, it was sufficient to obtain preliminary results and provide an early indication of the system’s performance.

Before characterizing the receiver’s performance, it was essential to first validate the single photon nature of the light source. This was accomplished by performing a photon antibunching measurement using a Hanbury Brown and Twiss (HBT) interferometer [5]. An HBT interferometer consists of a 50:50 non-polarizing BS with a single photon detector at each of its two output ports. The underlying principle is that a true single photon, upon entering the BS, cannot be split and must choose one of the two paths. Consequently, simultaneous detection events, or coincidences, at both detectors are suppressed at zero time delay. This behavior is quantified by the second-order autocorrelation function, $g^{(2)}(\tau)$. A value of $g^{(2)}(0) < 1$ is the signature of photon antibunching, with a value approaching zero indicating a high purity single photon source [9].

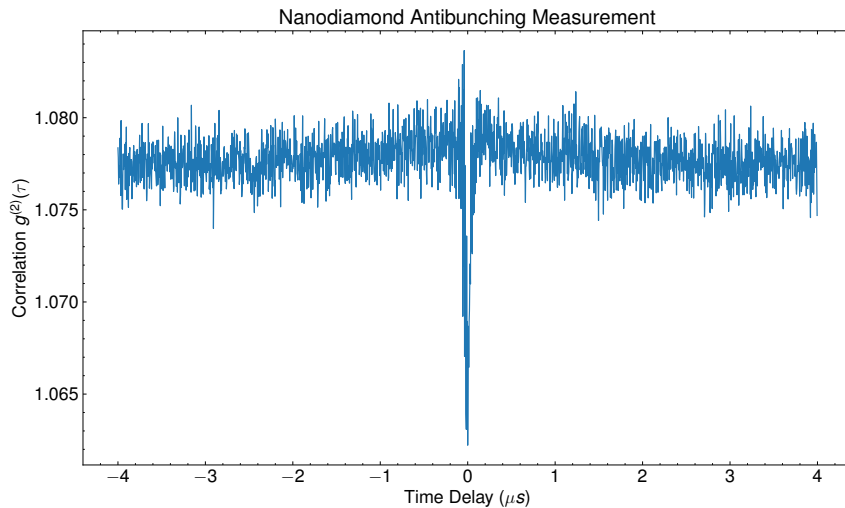


Figure 9: The graph shows the experimentally measured second-order autocorrelation function, $g^{(2)}(\tau)$, as a function of the time delay, τ .

The result of the antibunching measurement for the source based on NV centers is presented in Fig. 9. The data exhibits the characteristic dip in coincidence counts at zero time delay ($\tau = 0$), confirming a degree of antibunched light emission. However, the measured value of $g^{(2)}(0)$ did not fall below the commonly accepted threshold of 0.5 that is required to confidently classify the source as a single photon emitter. This elevated value was attributed to excessively high count rates, which likely indicates that either a non-ideal NV center was being excited or, more probably, that multiple centers were being excited simultaneously. Given that the source’s single photon purity could not be sufficiently verified, it was concluded that this source was suitable only for the initial system testing. It was not appropriate for the final QKD experiments planned for the future.

We began the system characterization using the single photons from the NV centers in nanodiamonds. As described previously in Section 3.3, we placed a linear polarizer at the system’s input to simulate the various polarization states that would be prepared by Alice.

The primary goal of this test was to confirm that the photon counts at each of the four output ports followed the expected sinusoidal pattern as the input polarization was rotated. This $\cos^2(\theta)$ behavior following Malus’s law is essential, as it verifies that the polarization analysis modules are working correctly. To gather this data, we measured the count rates at all four ports, then rotated the input polarizer by 10° and repeated the measurement. We continued this process until we had swept through a full 360° rotation.

The acquired photon count data was processed to calculate the normalized count rates for each orientation of the input polarizer. These results are presented in Fig. 10. The data confirms the expected theoretical behavior, showing a clear sinusoidal dependence of the count rates on the polarizer angle for all four output ports. This result validates the correct operation of the polarization analysis modules.

To illustrate this, consider the case where the input polarization is set to vertical (an angle of 180°). As shown in the Fig. 10, the count rate approaches its maximum value at the corresponding vertical detection port ($|V\rangle$) and, concurrently, its minimum value at the orthogonal horizontal detection port ($|H\rangle$). Under this same input condition, the rates at the diagonal ($|D\rangle$) and anti-diagonal ($|A\rangle$) ports are observed to be nearly equal and at an intermediate value, consistent with theoretical predictions for a measurement in a mismatched basis.

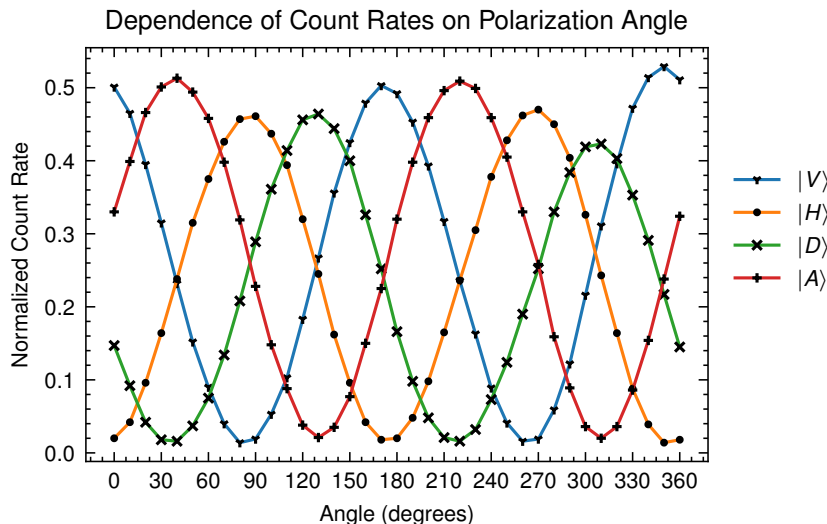


Figure 10: The plot shows the normalized count rates for the four detection ports as the input linear polarization is rotated through 360° . The data shown was obtained using the photon source based on NV centers.

During the initial characterization of the system with the photon source based on NV centers, a significant performance anomaly was identified, as shown in the data in Fig. 10. Although the expected sinusoidal dependence of count rates on the input polarization

was observed, the peaks of the curves for the four output ports did not reach a uniform maximum. This disparity indicated a substantial, underlying polarization dependent loss within the receiver itself. An initial hypothesis blaming a wavelength mismatch between the source and the optical coatings was refuted, as a similar power imbalance had also been noted during alignment with the visible laser. This confirmed the issue was a fundamental property of the setup that needed to be resolved.

To diagnose the source of this loss, a systematic investigation was undertaken using the alignment laser, with optical power measured sequentially after each component. This procedure conclusively demonstrated that the significant power loss occurred at the two dielectric steering mirrors positioned after the WPP in each measurement arm. Furthermore, the effect was dramatically more pronounced for the horizontally polarized beam paths. Quantitative measurements confirmed this, in a vertically polarized path, power decreased minimally from $82\mu\text{W}$ to $80.2\mu\text{W}$ after two reflections, while in the horizontal path, power dropped drastically from $50\mu\text{W}$ to just $11.6\mu\text{W}$.

This evidence leads to the conclusion that the dielectric mirrors used in the setup exhibit a strong polarization dependent reflectivity. This behavior is consistent with the well established principles of reflection from dielectric surfaces, where s-polarized and p-polarized light have different reflection coefficients [18]. The performance anomaly was therefore confidently attributed to this physical property of the mirrors. Understanding and quantifying this effect was a critical prerequisite before proceeding with characterization using the final BBO source.

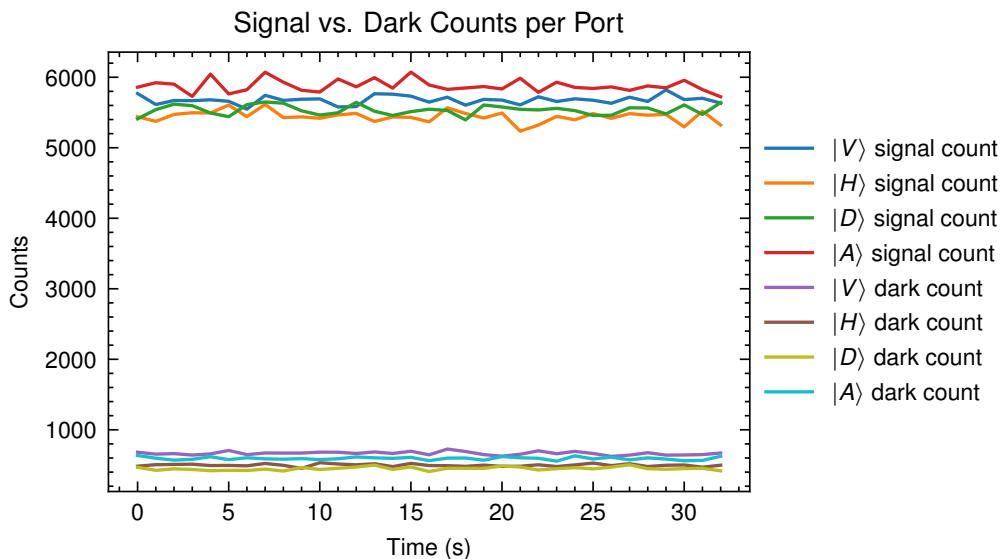


Figure 11: The graph compares the measured signal photon counts (with the BBO source active) to the intrinsic dark counts (with the source blocked) for each of the four output detection channels.

4.2 Final Performance Validation with the BBO Source

Prior to characterizing the full receiver system with the intended single photon source, baseline measurements were performed to establish both the source flux and the detector noise floor. To measure the raw photon output of the BBO crystal, a large core MMF was used to maximize collection efficiency by coupling the emission directly to the APD. This

test yielded count rates in the range of 136,000 - 140,000 counts per 1ns time bin, measured over 1000 bins. Subsequently, a dark count measurement was conducted by blocking the source to quantify the detector's intrinsic noise. As shown in Fig. 11, the dark count rate peaked at approximately 700 counts during this measurement. This confirms our detection system has a low noise floor. With these source and noise characteristics established, the BBO source was integrated with the receiver setup. The system's throughput was then optimized by systematically adjusting the steering mirrors to maximize the photon counts at each of the four output ports. Figure 11 presents the final, optimized signal count rates for each port, with all measured values ranging between 5,400 and 6,000 counts. While further optimization could potentially improve these rates, the characterization proceeded with the setup in this stable and well defined state due to practical and time related constraints.

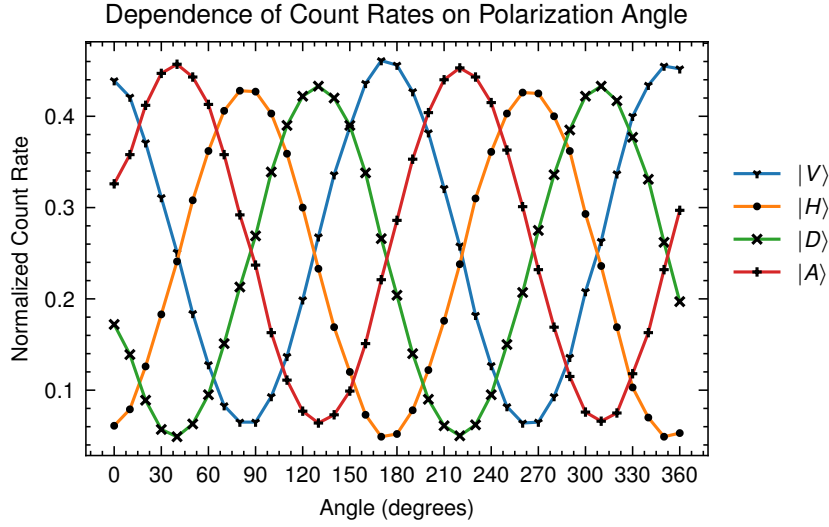


Figure 12: The plot shows the normalized count rates for the four detection ports as the input linear polarization is rotated through 360° . The data shown was obtained using the single photon source based on BBO crystal.

Finally, the system was characterized using the intended BBO single photon source. The measurement procedure was identical to the preliminary tests, the count rates at each port was recorded as a function of the input linear polarizer's angle, which was rotated through a full 360° . The results, presented in Fig. 12, successfully confirm the expected sinusoidal behavior for all four detection channels. Critically, and in contrast to the data from the nanodiamond source, the amplitudes of the count rates for all ports are now uniform. This outcome validates the hypothesis that the previously observed amplitude discrepancy was a wavelength dependent artifact of the mirrors, which is not prominent at the correct operational wavelength of 810nm.

While the primary issue of polarization dependent loss was resolved, a slight vertical offset between the sinusoidal curves for the respective ports is still observable in the data. This minor discrepancy is attributed not to a polarization effect, but to small, residual differences in the fiber coupling efficiencies at each of the four outputs. Although these efficiencies could be improved with further fine tuning, the overall performance demonstrated in these measurements was deemed sufficient. Therefore, the receiver is considered validated and ready for integration into the next stages of a QKD system development.

5 Conclusion

A modular optical receiver (Bob) for use in BB84 QKD systems was successfully designed and constructed. The system architecture meets the fundamental requirements for decoding the four BB84 polarization states, featuring a passive mechanism for random basis selection. This passive choice is implemented using a non-polarizing 50:50 BS, which directs incoming photons into one of two measurement basis paths.

Within each path, a WPP is employed to spatially separate the orthogonal polarization components. The WPP was specifically chosen over other components, such as PBSs, due to its significantly higher extinction ratio. This ensures a high purity separation of the polarization states, which is critical for minimizing errors. Finally, the four resulting beams, corresponding to the four possible input states, are routed via steering mirrors to their respective detection ports and coupled into optical fibers. A maximum coupling efficiency of 97.3 % and a minimum of 88.5 % were achieved across the output ports. This level of performance is well within the acceptable tolerance for the application and confirms the viability of the alignment methodology. This overall design provides a robust and effective solution for the receiver module in a QKD experiment.

The system's functionality was validated through characterization with two distinct photon sources. This process confirmed the setup's correct operational principles while also highlighting key performance limitations. During preliminary testing with the nanodiamond source, a significant polarization dependent loss was identified and attributed to the steering mirrors. As hypothesized, when the system was subsequently tested with the intended source, photons from the BBO crystal, this effect was substantially reduced, though a minor residual dependence was still observable.

The final characterization with the BBO source revealed a secondary, less significant anomaly, a static vertical offset between the probability curves of the four output ports. This effect, which was not prominent in the initial tests, is attributed to small, non-uniform fiber coupling efficiencies at each port rather than a fundamental polarization issue. While this indicates that the system's throughput could be improved with further fine tuning of the couplings, the overall characterization successfully confirmed the viability of the receiver design.

As for future work, the receiver system in its current state is ready for immediate deployment in free-space QKD applications. Furthermore, its use can be extended to fiber-based systems with the integration of a polarization controller at the input, this module would be necessary to correct for polarization fluctuations induced by the fiber optic quantum channel. Finally, the system's modular design provides wavelength flexibility, allowing it to be adapted for different single photon sources by simply replacing key optical components with versions having coatings optimized for the desired wavelength.

Bibliography

- [1] Michael Bass and Virendra N. Mahajan. *Handbook of Optics*. 3rd ed. New York: McGraw-Hill, 2010. ISBN: 978-0-07-149889-0.
- [2] Fabio Benatti et al., eds. *Quantum Information, Computation and Cryptography: An Introductory Survey of Theory, Technology and Experiments*. Vol. 808. Lecture Notes in Physics. Berlin, Heidelberg: Springer Berlin Heidelberg, 2010. ISBN: 978-3-642-11913-2 978-3-642-11914-9. DOI: [10.1007/978-3-642-11914-9](https://doi.org/10.1007/978-3-642-11914-9). URL: <https://link.springer.com/10.1007/978-3-642-11914-9> (visited on 06/15/2025).
- [3] Charles H. Bennett and Gilles Brassard. “Quantum Cryptography: Public Key Distribution and Coin Tossing”. In: *Theoretical Computer Science* 560 (2014), pp. 7–11. ISSN: 03043975. DOI: [10.1016/j.tcs.2014.05.025](https://doi.org/10.1016/j.tcs.2014.05.025).
- [4] David M. Benton. *Alignment of Optical Systems Using Lasers*. SPIE, Sept. 3, 2021. ISBN: 978-1-5106-4620-9. DOI: [10.1117/3.2603804](https://doi.org/10.1117/3.2603804). URL: <https://www.spiedigitallibrary.org/ebooks/SL/Alignment-of-Optical-Systems-Using-Lasers/eISBN-9781510646209/10.1117/3.2603804> (visited on 04/25/2025).
- [5] R. Hanbury Brown and R. Q. Twiss. “Correlation Between Photons in Two Coherent Beams of Light”. In: *Nature* 177.4497 (Jan. 1956), pp. 27–29. DOI: [10.1038/177027a0](https://doi.org/10.1038/177027a0).
- [6] Dagmar Bruß and G. Leuchs, eds. *Lectures on Quantum Information*. 1st ed. Wiley, Nov. 6, 2006. ISBN: 978-3-527-40527-5 978-3-527-61863-7. DOI: [10.1002/9783527618637](https://doi.org/10.1002/9783527618637). URL: <https://onlinelibrary.wiley.com/doi/book/10.1002/9783527618637> (visited on 06/15/2025).
- [7] Russell A. Chipman, Wai-Sze Tiffany Lam, and Garam Young. *Polarized Light and Optical Systems*. Optical Sciences and Applications of Light. Boca Raton London New York: CRC Press, 2019. 1 p. ISBN: 978-1-4987-0056-6 978-1-4987-0057-3 978-1-351-12907-7.
- [8] *Extinction Ratio | MEETOPTICS Academy*. URL: <https://www.meetoptics.com/academy/extinction-ratio> (visited on 06/29/2025).
- [9] Mark Fox. *Quantum Optics: An Introduction*. Oxford University Press Oxford, Apr. 27, 2006. ISBN: 978-0-19-856672-4 978-1-383-02962-8. DOI: [10.1093/oso/9780198566724.001.0001](https://doi.org/10.1093/oso/9780198566724.001.0001). URL: <https://academic.oup.com/book/54796> (visited on 06/23/2025).
- [10] Nicolas Gisin et al. “Quantum Cryptography”. In: *Reviews of Modern Physics* 74.1 (Mar. 8, 2002), pp. 145–195. DOI: [10.1103/RevModPhys.74.145](https://doi.org/10.1103/RevModPhys.74.145). URL: <https://link.aps.org/doi/10.1103/RevModPhys.74.145> (visited on 06/13/2025).
- [11] Eugene Hecht. *Optics*. 5 edition. Global edition. Boston: Pearson Education, Inc, 2017. 1 p. ISBN: 978-0-13-397722-6 978-1-292-09696-4.
- [12] Tobias Schmitt Manderbach. “Long Distance Free-Space Quantum Key Distribution”. Ludwig-Maximilians-Universität München, Oct. 16, 2007.
- [13] Donald C. O’Shea. *Elements of Modern Optical Design*. 6. Dr. Wiley Series in Pure and Applied Optics. New York: Wiley, 1985. 402 pp. ISBN: 978-0-471-07796-1.
- [14] Sébastien Pezzagna et al. “Creation and Nature of Optical Centres in Diamond for Single-Photon Emission—Overview and Critical Remarks”. In: *New Journal of Physics* 13.3 (Mar. 2011), p. 035024. ISSN: 1367-2630. DOI: [10.1088/1367-2630/13/3/035024](https://doi.org/10.1088/1367-2630/13/3/035024). URL: <https://dx.doi.org/10.1088/1367-2630/13/3/035024> (visited on 06/17/2025).
- [15] Bahaa E. A. Saleh and Malvin Carl Teich. *Fundamentals of Photonics*. Third edition. Hoboken, NJ: Wiley, 2019. 1 p. ISBN: 978-1-119-50687-4 978-1-118-77009-2.

- [16] John M. Senior and M. Yousif Jamro. *Optical Fiber Communications: Principles and Practice*. 3rd ed. Harlow, England ; New York: Financial Times/Prentice Hall, 2009. 1075 pp. ISBN: 978-0-13-032681-2.
- [17] W. K. Wootters and W. H. Zurek. “A Single Quantum Cannot Be Cloned”. In: *Nature* 299.5886 (Oct. 1982), pp. 802–803. ISSN: 1476-4687. DOI: [10.1038/299802a0](https://doi.org/10.1038/299802a0). URL: <https://www.nature.com/articles/299802a0> (visited on 06/09/2025).
- [18] Yuzhe Xiao et al. “Lateral Beam Shifts and Depolarization Upon Oblique Reflection from Dielectric Mirrors”. In: *Annalen der Physik* 536.6 (2024), p. 2400028. ISSN: 1521-3889. DOI: [10.1002/andp.202400028](https://doi.org/10.1002/andp.202400028). URL: <https://onlinelibrary.wiley.com/doi/abs/10.1002/andp.202400028> (visited on 06/20/2025).

A Light in Anisotropic Media

This section reviews the principles governing the propagation of polarized light through anisotropic crystals. A thorough understanding of these concepts is essential, as the optical system developed in this work relies on components fabricated from such materials. The central phenomenon to be discussed is birefringence, which is the physical effect leveraged to control and analyze polarization states in our application.

A.1 Birefringence

Optical anisotropy is a material property characterized by a directionally dependent response to incident light, which arises from an asymmetric arrangement of atoms in the crystal's structure. To understand how this property affects light propagation, one must first consider the origin of a material's refractive index. The refractive index is fundamentally a consequence of the interaction between the light's electric field and the material's atomic electrons. The field drives the electrons into oscillation, and these oscillating electrons reradiate, forming the collective wave that propagates through the medium. The speed of this wave, and thus the refractive index, is determined by the relationship between the light's frequency and the natural resonant frequencies of the electrons[11].

In an anisotropic crystal, the forces binding the electrons to their equilibrium positions are not uniform in all directions. This can be conceptualized by modeling an electron as a mass attached to springs of differing stiffness; a displacement along a stiff axis will result in a different natural oscillation frequency than a displacement along a soft axis. Because the natural frequencies are direction dependent, and the refractive index is sensitive to these frequencies, the refractive index itself becomes directionally dependent. This phenomenon, where the refractive index experienced by light depends on its polarization and direction of propagation, is known as birefringence [11].

Furthermore, even within a birefringent crystal, there exists at least one specific direction along which this anisotropy vanishes. When light propagates along this direction, its orthogonal polarization components experience the same refractive index, and thus, no birefringence is observed. This unique direction of propagation is defined as the optic axis of the crystal.

The interaction of light with an anisotropic medium is mathematically described by the relationship between the induced material polarization, $\mathbf{P}(\mathbf{r}, \omega)$, and the applied electric field, $\mathbf{E}(\mathbf{r}, \omega)$. In component form, this relationship is expressed as:

$$P_i(\mathbf{r}, \omega) = \epsilon_0 \sum_{j=1}^3 \chi_{ij}(\omega) E_j(\mathbf{r}, \omega) \quad (9)$$

In this expression, the electric susceptibility, $\chi_{ij}(\omega)$, is a second rank tensor that encapsulates the structural properties of the crystal. A fundamental consequence of this tensorial relationship is that the polarization, $\mathbf{P}(\mathbf{r}, \omega)$, is not necessarily parallel to the electric field vector, $\mathbf{E}(\mathbf{r}, \omega)$. This anisotropy also defines the constitutive relation between the electric displacement field, $\mathbf{D}(\mathbf{r}, \omega)$, and the electric field, which is given by,

$$\mathbf{D}(\mathbf{r}, \omega) = \epsilon_0 \mathbf{E}(\mathbf{r}, \omega) + \mathbf{P}(\mathbf{r}, \omega) \quad (10)$$

$$= \epsilon_0 \mathbf{E}(\mathbf{r}, \omega) + \epsilon_0 \chi \mathbf{E}(\mathbf{r}, \omega) \quad (11)$$

$$= \epsilon_0 (1 + \chi) \mathbf{E}(\mathbf{r}, \omega) \quad (12)$$

$$= \epsilon_0 \epsilon_r \mathbf{E}(\mathbf{r}, \omega) \quad (13)$$

$$= \epsilon \mathbf{E}(\mathbf{r}, \omega) \quad (14)$$

This leads to the constitutive relation for the electric displacement field, $\mathbf{D}(\mathbf{r}, \omega)$, in an anisotropic medium,

$$D_i(\mathbf{r}, \omega) = \epsilon_0 \sum_{j=1}^3 \epsilon_{ij}(\omega) E_j(\mathbf{r}, \omega) \quad (15)$$

$$\mathbf{D}(\mathbf{r}, \omega) = \epsilon_0 \hat{\epsilon}(\omega) \mathbf{E}(\mathbf{r}, \omega) \quad (16)$$

Here, the medium's optical response is encapsulated in the dielectric tensor, $\hat{\epsilon}$. Just as the polarization \mathbf{P} can be non-parallel to \mathbf{E} , this tensorial form implies that the electric displacement field \mathbf{D} may also not be collinear with the electric field.

In the principal coordinate system of an anisotropic crystal, the dielectric tensor $\hat{\epsilon}$ takes on a simple diagonal form, with its principal axes aligned with the coordinate axes [7]. This simplifies the relationship between the electric displacement \mathbf{D} and the electric field \mathbf{E} to three independent equations along these axes [15],

$$D_1 = \epsilon_1(\omega) E_1, \quad D_2 = \epsilon_2(\omega) E_2, \quad D_3 = \epsilon_3(\omega) E_3 \quad (17)$$

where the principal permittivities

$$\epsilon_1 = \epsilon_{11}, \quad \epsilon_2 = \epsilon_{22}, \quad \epsilon_3 = \epsilon_{33}$$

are the diagonal tensor elements.

$$\begin{bmatrix} D_1 \\ D_2 \\ D_3 \end{bmatrix} = \begin{bmatrix} \epsilon_1(\omega) & 0 & 0 \\ 0 & \epsilon_2(\omega) & 0 \\ 0 & 0 & \epsilon_3(\omega) \end{bmatrix} \begin{bmatrix} E_1 \\ E_2 \\ E_3 \end{bmatrix} \quad (18)$$

The inverse of the dielectric tensor, $\hat{\epsilon}(\omega)$, is defined as the electric impermeability tensor, $\hat{\sigma}(\omega)$. The resulting relationship is given by,

$$\epsilon_0 \mathbf{E}(\mathbf{r}, \omega) = \hat{\epsilon}^{-1}(\omega) \mathbf{D}(\mathbf{r}, \omega) \quad (19)$$

$$\hat{\sigma}(\omega) = \hat{\epsilon}^{-1}(\omega) \quad (20)$$

Index Ellipsoid The electric impermeability tensor can be represented geometrically by a surface in three-dimensional space known as the index ellipsoid, which is defined by the following equation [15],

$$\sum_{i,j=1}^3 \sigma_{ij} x_i x_j = 1, \quad i, j = 1, 2, 3 \quad (21)$$

$$\sigma_{11}x_1^2 + \sigma_{22}x_2^2 + \sigma_{33}x_3^2 = 1 \quad (22)$$

$$\frac{x_1^2}{\epsilon_1} + \frac{x_2^2}{\epsilon_2} + \frac{x_3^2}{\epsilon_3} = 1 \quad (23)$$

$$\frac{x_1^2}{n_1^2} + \frac{x_2^2}{n_2^2} + \frac{x_3^2}{n_3^2} = 1 \quad (24)$$

where $n_i = \sqrt{\epsilon_i}$ are the principal refractive indices. As illustrated in Fig. 13, the vector $\hat{\mathbf{u}} = \frac{\mathbf{k}}{k}$ is the unit vector that defines the direction of wave propagation within the anisotropic material.

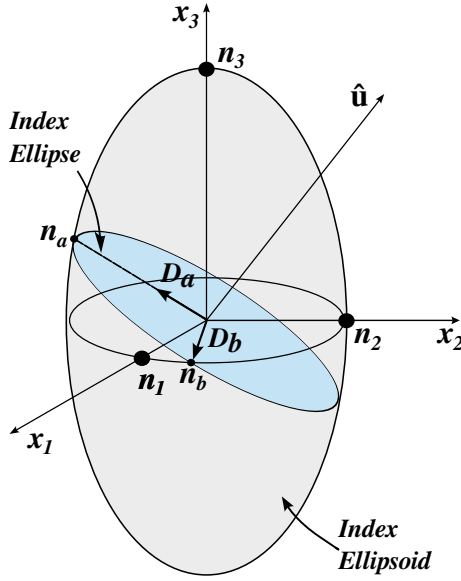


Figure 13: Index ellipsoid. Adapted from [15].

B Fiber Coupling

Fiber coupling is a fundamental technique in optics, utilized in a wide range of laboratory applications. The process involves efficiently focusing a free-space light beam into the core of an optical fiber. In a typical configuration, a lens is used to match the profile of an incident Gaussian beam to the fiber core, as illustrated in Fig. 14. This task is particularly delicate and requires high precision due to the microscopic length scales involved.

The challenge is especially pronounced when working with SMF, as opposed to MMF. A single-mode fiber can have a core diameter as small as $8\mu m$, which makes precise alignment and efficient power transfer a difficult problem. Therefore, the selection of an appropriate lens is critical for successful coupling and depends on several key parameters:

- wavelength (λ)
- collimated beam diameter incident on the coupling lens (D)

- NA
- mode field diameter (MFD)

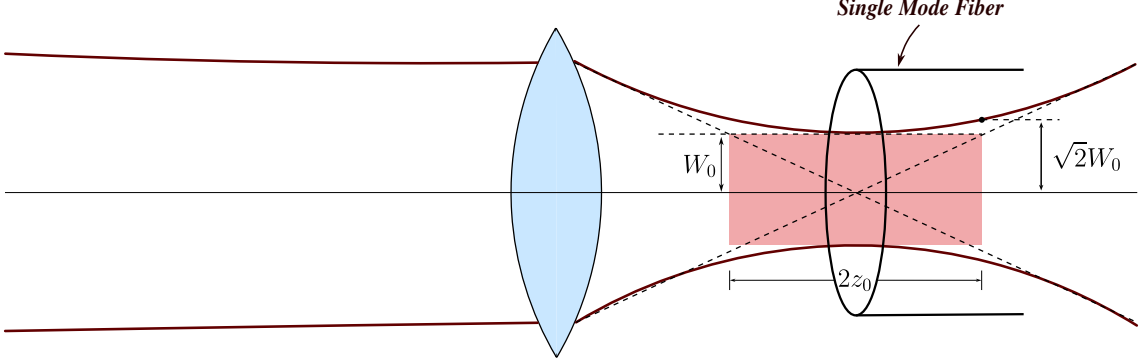


Figure 14: Focusing a Gaussian beam into a single mode fiber using a lens of focal length f .

For a specific application, the appropriate focal length, f , can be determined using the following equation [13],

$$f = \frac{\pi \cdot D \cdot MFD}{4 \cdot \lambda} \quad (25)$$

Beam Waist The beam width of the Gaussian beams are expressed with the following relation,

$$W(z) = W_0 \sqrt{1 + \left(\frac{z}{z_0}\right)^2} \quad (26)$$

The beam waist, W_0 , represents the minimum radius of the beam.

Rayleigh Range The Rayleigh range (z_0) specifies the length of a beam's collimated region. It is defined as the distance from the beam waist where the cross-sectional area doubles, meaning its radius expands to $\sqrt{2}W_0$ as depicted in Fig. 14 [13]. The expression of the Rayleigh range is given by,

$$z_0 = \frac{\pi W_0^2}{\lambda} \quad (27)$$

Numerical Aperture The **numerical aperture** of an optical fiber is a key parameter that quantifies its light gathering ability. To derive its mathematical expression, we consider the configuration shown in Fig. 15, where a fiber with core refractive index n_f and cladding index n_c is placed in a medium of index n_i . The derivation is based on the fiber's acceptance angle, θ_{max} , which represents the maximum incident half angle for which light will be guided via **TIR** [11]. The derivation proceeds as follows,

$$\begin{aligned} \sin \theta_c &= n_c/n_f = \sin(90^\circ - \theta_t) \\ n_c/n_f &= \cos \theta_t \\ n_c/n_f &= (1 - \sin^2 \theta_t)^{1/2} \end{aligned}$$

Finally, by applying Snell's law, we obtain the expression for the **numerical aperture**,

$$NA = n_i \sin \theta_{max} = (n_f^2 - n_c^2)^{1/2} \quad (28)$$

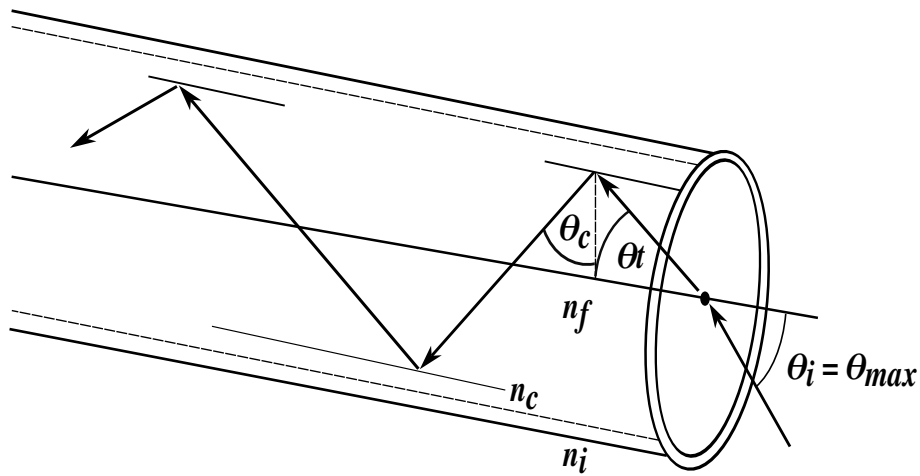


Figure 15: The acceptance angle and general structure of an optical fiber. The diagram shows the fiber's core and cladding, and illustrates the maximum acceptance angle, θ_{max} . Adapted from [11].

Mode Field Diameter In a **single-mode fiber**, the guided light is not strictly confined within the physical core, a fraction of its electromagnetic field propagates within the cladding as an evanescent wave. Consequently, the effective diameter of this intensity profile, termed the **mode field diameter**, is typically larger than the core diameter itself. The **MFD** is quantified as twice the radial distance at which the beam's intensity drops to $1/e^2$ of its peak intensity.

Acknowledgements

I wish to thank my supervisor, Dr. José María Gómez Cama, for their guidance, and my group leader, Prof. Dr. Bruno Julia Díaz, for their support. My sincere thanks to Lidia Lozano Martín, Raul Lahoz Sanz, and Lucía Guerrero Muñoz for their valuable discussions and support.

This study was supported by MCIN with funding from European Union NextGenerationEU (PRTR-C17.I1) and by Generalitat de Catalunya. We acknowledge funding from Grants PID2023-147475NB-I00 and CEX2024-001451-M financed by MCIN/AEI/10.13039/501100011033 and Grants 2021SGR01095, and 2021SGR01108 by Generalitat de Catalunya. This project has received funding from the European Union's Digital Europe Programme under grant agreement no. 101084035.